submitted to **Journal of Space Weather and Space Climate**

The spheroid CME model in EUHFORIA

Camilla Scolini[1,2] and Erika Palmerio[3]

[1] Solar–Terrestrial Centre of Excellence—SIDC, Royal Observatory of Belgium, 1180 Brussels, Belgium
e-mail: camilla.scolini@oma.be
[2] Space Science Center, University of New Hampshire, Durham, NH 03824, USA
[3] Predictive Science Inc., San Diego, CA 92121, USA

Received September 16, 2023; revised April 3, 2024; accepted April 4, 2024

ABSTRACT

Predictions of coronal mass ejection (CME) propagation and impact in the heliosphere, in either research or operational settings, are usually performed by employing magnetohydrodynamic (MHD) models. Within such simulations, the CME ejecta is often described as a hydrodynamic pulse that lacks an internal magnetic field and is characterized by a spherical geometry—leading to the so-called cone CME model. White-light observations of CMEs in the corona, however, reveal that the morphology of these structures resembles more closely that of a croissant, i.e., exhibiting an elongated cross section of their front. It follows that, in space weather forecasts, the assumption of a spherical geometry may result in erroneous predictions of CME impacts in the heliosphere in terms of hit/miss and arrival time/speed, especially in the case of flank encounters. A spheroid CME model is expected to provide a more accurate description of the elongated morphology that is often observed in CMEs. In this paper, we describe the implementation and initial validation of the spheroid CME model within the MHD EUropean Heliospheric FORecasting Information Asset (EUHFORIA) code. We perform EUHFORIA simulations of an idealized CME as well as a "real" event to compare the spheroidal model with the traditional cone one. We show how the initial ejecta geometry can lead to substantially different estimates in terms of CME impact, arrival time/speed, and geoeffectiveness, especially with increasing distance to the CME nose.

Key words. Coronal Mass Ejections – Space Weather Predictions – Magnetohydrodynamics

1. Introduction

Coronal mass ejections (CMEs) are among the most severe drivers of geomagnetic effects at Earth and, as such, are routinely monitored, analyzed, and modeled by space weather forecasting agencies (e.g., Pizzo et al., 2011). Once a CME erupts, its geometric and kinematic properties are usually estimated from white-light coronagraph imagery, and the resulting set of parameters is employed as input for magnetohydrodynamic (MHD) models of CME propagation in the inner heliosphere. A variety of models have been developed to describe CME structures in the context of heliospheric MHD models, including magnetized flux-rope models that account for various geometrical and magnetic

This provisional PDF is the accepted version. The article should be cited as: J. Space Weather Space Clim., doi: 10.1051/swsc/2024011

field descriptions of CMEs (see, e.g. Kataoka et al., 2009; Zhou et al., 2014; Zhang et al., 2019; Singh et al., 2020; Shen et al., 2021a,b; Maharana et al., 2022). However, for the purpose of operational space weather forecasting, CMEs in MHD models are typically treated without an internal magnetic field description, i.e., the injected structure is simplified as a hydrodynamic cloud or pulse (e.g., Odstrcil, 2003; Pomoell and Poedts, 2018). This approach—despite yielding not fully realistic CME interactions with the ambient solar wind and/or other solar transients—not only allows for more rapid predictions in terms of computational time, but also avoids the complex description of the magnetic configuration of the embedded flux rope, which is more difficult to characterize in real time (e.g., Kilpua et al., 2019). The three-dimensional (3-D) de-projected geometric and kinematic properties of CMEs in the corona are usually derived via triangulation techniques, such as the Space Weather Prediction Center CME Analysis Tool (SWPC-CAT; Millward et al., 2013, commonly employed in operational settings) and the Graduated Cylindrical Shell (GCS; Thernisien, 2011, widely used in the research community) model.

When observed in the solar corona, CMEs often exhibit an elongated cross section of their front, leading to a so-called "croissant" morphology that is often associated with an internal flux rope structure (e.g., Cremades and Bothmer, 2004; Vourlidas et al., 2013). To take this aspect into account, many forward models employed in CME research—such as the GCS technique mentioned above, or the coronagraph fitting tool implemented within the Flux Rope in 3D (FRi3D; Isavnin, 2016) architecture—are described by a number of free parameters that allow for a toroidal axis of the structure and two well-separated legs that connect back to the Sun. However, these models are only meant to reproduce the morphology of CMEs in the corona, and thus consist of "hollow" parameterized shells, with no information on the internal magnetic configuration—especially since coronal fields cannot be measured routinely at present. On the other hand, these reconstruction techniques permit relatively quick estimates of the geometric and kinematic properties of CMEs using one or more viewpoints, and their outputs can be directly employed in CME propagation models, either on their own (leading to the injection of an hydrodynamic pulse as described above) or combined with indirect information on the magnetic field of the corresponding flux rope (e.g., from solar disk observations; Palmerio et al., 2017).

The CME geometry assumed by most CME propagation models themselves (especially those used in forecasting), however, is much simpler, and is typically described as a spherical shape. In other words, these models are significantly more compatible with the geometry of the so-called "ice-cream cone" (Fisher and Munro, 1984) description of CMEs than with that of the croissant—which, on the other hand, is generally regarded as more realistic. An example of a CME reconstructed using white-light data employing both the cone and croissant models is shown in Figure 1. When adapting fitting results based on coronagraph imagery to CME propagation models that assume a spherical morphology, there are two possible approaches. The first is to reconstruct the CME by applying directly the cone model (e.g., Palmerio et al., 2019; Scolini et al., 2019), while the second is to first use the croissant model and then derive a circular front by considering, e.g., the maximum elongation or the average radius of the resulting structure (e.g., Scolini et al., 2020; Asvestari et al., 2021). Either way, not accounting for the observed elongation in the CME frontal cross section can result in wrong predictions of a CME's impact at a certain location in terms of its hit/miss outcome, as well as of its arrival time and/or speed, especially in the case of glancing encounters. A prominent example is that of the 7 January 2014 event (featured in Figure 1), whose interplanetary propagation was studied in detail by Mays et al. (2015) and Möstl et al. (2015). This CME, despite

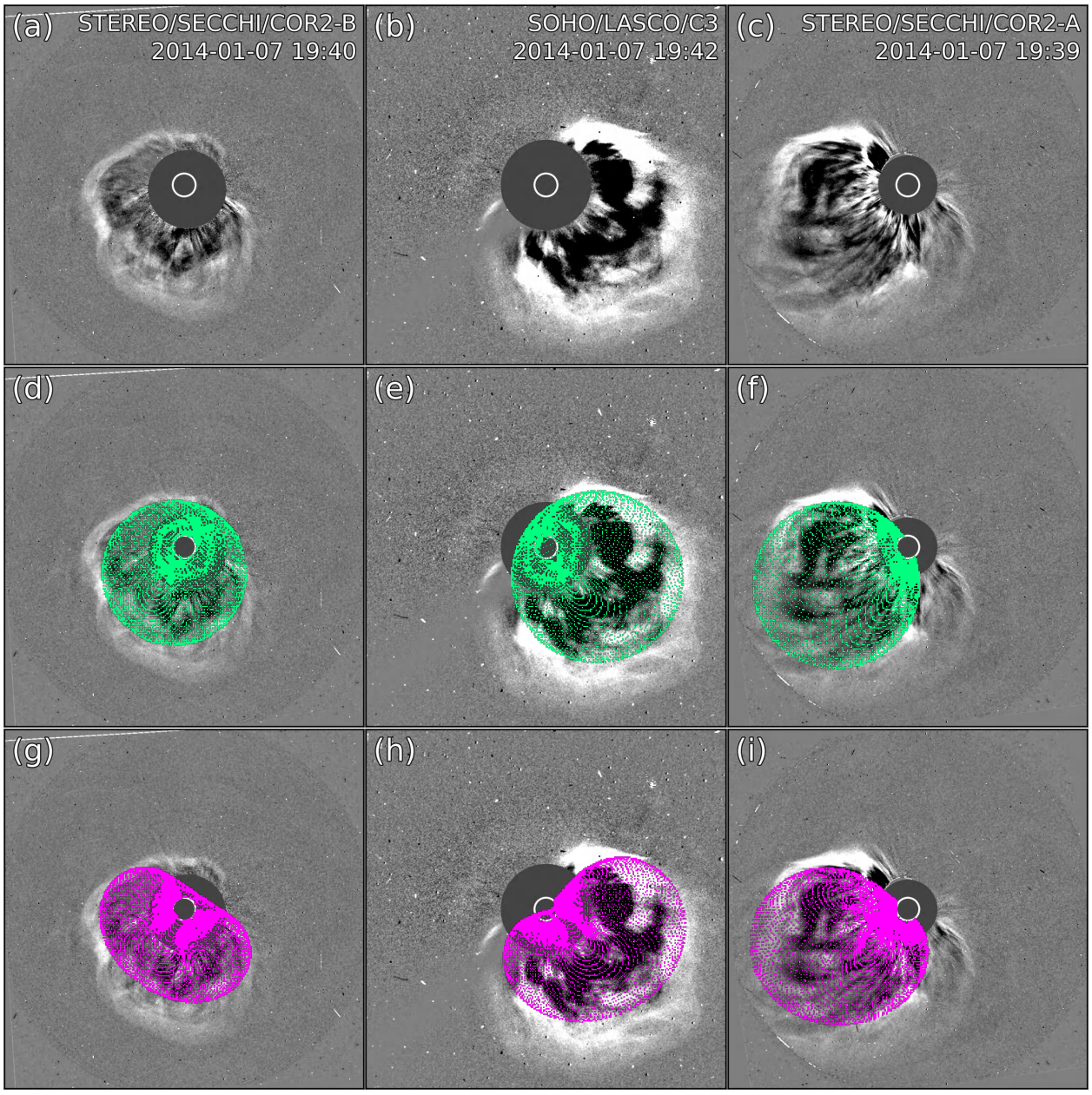

Fig. 1. Example of a CME (from 7 January 2014) fitted in the solar corona using the cone and croissant models. The top row (a–c) shows white-light data from three viewpoints (Earth/SOHO, STEREO-A, and STEREO-B), the middle row (d–f) shows the same set of data with the cone wireframe (in green) overlaid, and the bottom row (g–i) shows the same set of data with the croissant wireframe (in magenta) overlaid. Both sets of reconstructions were performed using the GCS model, with the difference that for the cone case the so-called half-width parameter (quantifying the half-angular separation between the CME legs) was set to zero.

originating from the vicinity of the central meridian of the Earth-facing Sun and being very fast and energetic, experienced a strong westward deflection in the solar corona and resulted only in a flank

encounter at Earth. Mays et al. (2015) showed that, in this case, hindcasts that assumed a spherical CME geometry performed significantly worse than those that employed a tilted ellipsoidal CME morphology.

In this work, we focus on the MHD EUropean Heliospheric FORecasting Information Asset (EUHFORIA; Pomoell and Poedts, 2018) model. Specifically, to improve current EUHFORIA space weather research and forecasting capabilities, we have increased the flexibility of the (default) cone model by introducing the modeling of CME geometry as a spheroid. In this paper, we report the details of such a new capability and present a first validation, which is achieved through comparison with the standard cone model and with in-situ signatures (typical CME or well-studied event). The paper is structured as follows. Section 2 presents a technical description of the model implementation. Section 3 presents a first validation of the model capabilities for a hypothetical (idealized) CME event, while Section 4 present the improvement in the case of a real CME event observed on 7 January 2014 and previously studied by Mays et al. (2015). Section 5 summarizes our conclusions and future perspectives.

2. Spheroid CME model implementation

The spheroid CME model is a spheroid-shaped hydrodynamical CME model, similar to the "traditional" cone model described by Pomoell and Poedts (2018). The CME is assumed to propagate radially outwards from the source location with a uniform speed, density, and temperature throughout. Similarly to the traditional cone model, the spheroidal model requires as input the following geometric and kinematic parameters at 0.1 au (i.e., the heliospheric inner boundary of EUHFORIA): the latitude and longitude of the CME center (θ_{CME} and ϕ_{CME}, in HEEQ coordinates), the speed of the CME (v_{CME}, in km s^{-1}), and the time at which the CME front first intersects the model inner boundary (t_{CME}). However, while the cone model traditionally assumes a spherical CME shape, the newly-implemented spheroidal model allows for a more accurate description of the elongated morphology that is often observed in CMEs. Thus, while the cone model only requires the half-angular width as input parameter ($\omega_{\mathrm{CME}}/2$, in degrees), the spheroidal model introduced here requires three parameters to characterise a given CME's geometry: the semi-major axis (r_{maj}, in solar radii, R_s), the semi-minor axis(r_{min}, in R_s), and the tilt angle (γ_{CME}, in degrees and computed anti-clockwise from the solar west direction as seen from the equatorial plane). In addition to the aforementioned set of geometrical and kinematic parameters, the spheroidal CME model also assumes a homogeneous density (ρ_{CME}) and temperature (T_{CME}) as does the traditional cone model.

We note that in the traditional cone model first introduced in its EUHFORIA implementation by Pomoell and Poedts (2018), the conversion from the CME angular width to the CME radius in the code is implemented based on the tangent relation (Equation 1 in Scolini et al., 2018b). For the purpose of directly comparing with the traditional cone model, here we decide to keep this relation to operate the translation between the angular width and the radius of the CME at 0.1 au in the spheroidal model as well, although a more appropriate alternative is provided by Equation 2 in Scolini et al. (2018b).

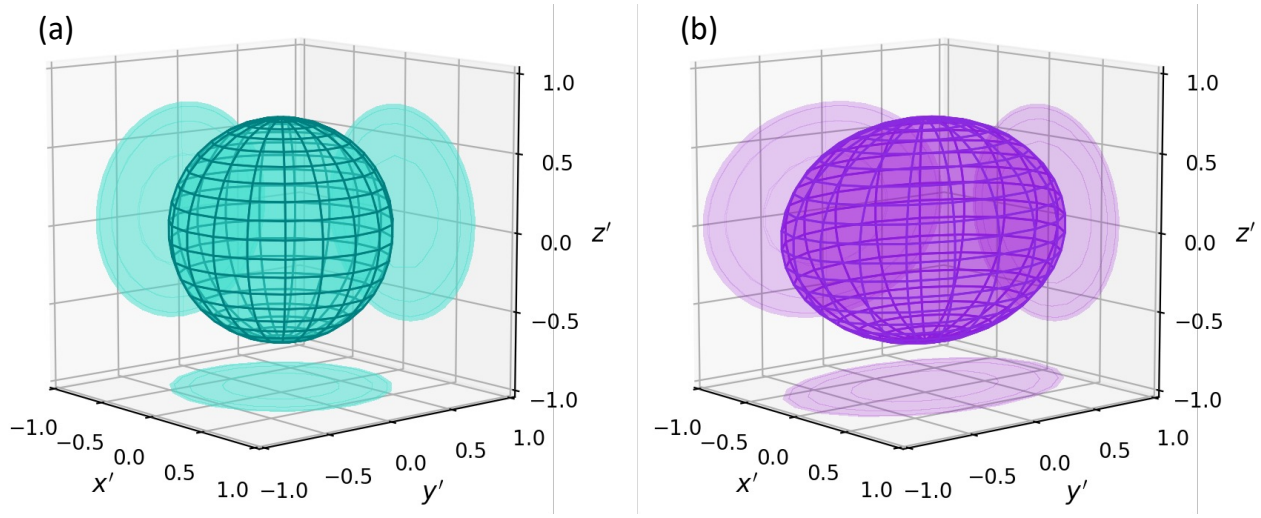

Fig. 2. 3-D visualization of the (a) spherical and (b) spheroidal CME shapes. x', y', and z' constitute a local coordinate system centered at the center of the CME. Dimensions are normalized to 1 for convenience. The spherical CME has circular cross sections in the directions perpendicular to x', y', and z', as shown by the 2-D shadow projections. The spheroidal CME has a circular cross sections only in the direction perpendicular to the major axis (parallel to y'), while it has elliptical cross sections in the directions perpendicular to the minor axes (parallel to x' and z'), as shown by the 2-D shadow projections.

In detail, for each (θ, ϕ) cell part of the inner boundary of the model domain, the polar angle with respect to the CME center is computed as

$$\theta'(\theta,\phi) = \arctan\left(\frac{\theta - \theta_{\mathrm{CME}}}{\phi - \phi_{\mathrm{CME}}}\right). \tag{1}$$

Then, a static mask (in units of R_s) is introduced to identify which cells on the inner boundary are going to be part of the CME frontal cross section during the insertion period, as follows:

$$\mathrm{mask}_{Rs}(\theta,\phi) = \frac{r_{\mathrm{min}} r_{\mathrm{maj}}}{\sqrt{(r_{\mathrm{min}}^2 - r_{\mathrm{maj}}^2)\cos^2(\theta'(\theta,\phi) - \gamma_{\mathrm{CME}}) + r_{\mathrm{maj}}^2}}. \tag{2}$$

The normalization to radians is performed as

$$\mathrm{mask}_{\mathrm{rad}}(\theta,\phi) = \arctan\left(\frac{\mathrm{mask}_{Rs}(\theta,\phi)}{21.5\,R_s}\right). \tag{3}$$

The time dependence of the mask is obtained multiplying the static mask by a time-dependent "normalized opening angle" (running between 0 and 1), similarly to what done for the traditional cone model in EUHFORIA (Pomoell and Poedts, 2018; Scolini et al., 2018b):

$$\mathrm{mask}_{\mathrm{rad}}(\theta,\phi,t) = \mathrm{mask}_{\mathrm{rad}}(\theta,\phi)\cdot\zeta(t) = \mathrm{mask}_{\mathrm{rad}}(\theta,\phi)\cdot\sin\left(\frac{\pi}{2}\frac{t}{t_{1/2}}\right), \tag{4}$$

where $t_{1/2} = r_{\rm min}/v_{\rm CME}$ is the time at which the CME geometrical center crosses the inner boundary. We impose that at any given time t during the CME insertion period, all (θ, ϕ) points on the inner boundary that satisfy the condition

$$(\theta - \theta_{\rm CME})^2 + (\phi - \phi_{\rm CME})^2 < {\rm mask}^2_{\rm rad}(\theta, \phi, t) \quad (5)$$

are inside the CME, while all that do not satisfy this relation are outside of the CME. At each point within the CME, the speed, density, and temperature are initialized to the $v_{\rm CME}$, $\rho_{\rm CME}$, and $T_{\rm CME}$ specified by the user. For each point outside of the CME, the values are retained to those of the ambient solar wind. Because this is an unmagnetized CME model, for all points the magnetic field conditions are retained to those of the ambient solar wind.

As a result, in the spheroidal model CMEs have a spherical cross section only in the r–θ plane, while they have elliptical cross sections when sliced in θ–ϕ surfaces of constant r. Figure 2 provides a 3-D visualization of the geometry of a spherical and spheroidal CME shape, as well as a projection of their cross sections onto the various planes (for a Cartesian coordinate system x', y', and z' centered at the CME center).

3. Spheroid CME model validation: fictitious CME event

To exemplify the similarities between the cone and spheroidal CME models, as well as to highlight the advantages associated with the use of a spheroidal model over the cone model under certain circumstances, we simulate hypothetical CME events propagating through a synthetic solar wind background. This solar wind background is the same as previously employed by Scolini et al. (2021, 2023), and it includes a heliospheric current and plasma sheet with sinusoidal behaviour in longitude which reaches up to ±15° in latitude. The solar wind has a baseline value of 450 km s^{-1} (intermediate between slow and fast solar wind) everywhere except for regions around the plasma sheet, where the speed reaches values as low as 300 km s^{-1}. Full details are provided by Scolini et al. (2021, 2023), while a 2-D full view of the solar wind mass density and magnetic field boundary conditions is provided in Figure 1 by Scolini et al. (2021). Characterizing the behavior of this newly-implemented spheroidal CME model in EUHFORIA in such an idealized solar wind condition represents a first but necessary step to later be able to conduct a meaningful interpretation of the results obtained for CME structures propagating through different (incl. more realistic, see Section 4) solar wind conditions.

We run the same fictitious CME event with both the cone and spheroidal models, using input parameters as similar as possible. The complete set of input CME parameters at 21.5 R_s used to initialize the EUHFORIA runs is listed in Table 1. For the spheroidal model, we choose the major axis to be aligned with the equatorial plane (corresponding to a tilt angle of $\gamma_{\rm CME} = 0°$), so that the advantage of using a spheroidal CME geometry is maximal in the region around to the ecliptic plane (i.e., where most planets, as well as most past and currently operational spacecraft probing the solar wind conditions are located).

In addition to the input parameters required by EUHFORIA, the bottom portion of Table 1 lists some derived parameters, namely the CME total volumes ($V_{\rm CME}$), masses ($m_{\rm CME}$), and kinetic energies ($E_{\rm kin,CME}$). As a result of the choices of input parameters, these differ by less than 2% in the two models, and they are representative of the typical population of fast CMEs observed in Solar Cycles 23 and 24 (Gopalswamy, 2006; Jang et al., 2016; Lamy et al., 2019). Despite the idealized

	Spherical (cone) model	Spheroidal model
t_{CME}	2023-01-01 00:00 UT	2023-01-01 00:00 UT
ϕ_{CME}	0°	0°
θ_{CME}	0°	0°
v_{CME}	800 km s^{-1}	800 km s^{-1}
γ_{CME}	–	0°
$\omega_{\mathrm{CME}}/2$	25° (10.02 R_s)	–
r_{maj}	–	37° (16.20 R_s)
r_{min}	–	20° (7.82 R_s)
ρ_{CME}	1×10^{-18} kg m^{-3}	1×10^{-18} kg m^{-3}
T_{CME}	0.8×10^{6} K	0.8×10^{6} K
V_{CME}	1.42×10^{30} m^3	1.40×10^{30} m^3
m_{CME}	1.42×10^{12} kg	1.40×10^{12} kg
$E_{kin,\mathrm{CME}}$	4.55×10^{23} J	4.48×10^{23} J

Table 1. CME input parameters used for the spherical (cone) and spheroidal models to initialize the fictitious CME cases.

numerical set-up employed in this fictitious CME experiment, we therefore expect the results to apply to a potentially large set of real CME events. In the spheroidal model, we set r_{maj} to be twice as large as r_{min}, so that the CME aspect ratio is 2:1 in the longitudinal versus latitudinal directions.

3.1. Comparison with the spherical (cone) model at 0.1 au

Figure 3 shows the radial speed and particle number density at the inner boundary (r = 0.1 au) during the CME insertion period for the cone and spheroidal simulations. The area where the CME is being inserted (v_r = 800 km s^{-1}, n = 600 cm^{-3}) is visible as the red (orange) patch on the left (right). The CME cross section appears visibly different between the two runs, especially in the longitudinal direction where the CME has a radius of 10.02 R_s in the cone model run, and of 16.20 R_s in the spheroidal model run. On the other hand, in the latitudinal direction the two CME present a more similar extension, as dictated by their radius of 10.02 R_s in the cone model run and of 7.82 R_s in the spheroidal model run.

As a result, even if the injected CMEs are both centered on the fictitious Sun–Earth line, the spheroid one is expected to be better suited to reproduce in-situ arrivals across a wider range of heliolongitudes—particularly amenable for flank encounters and multi-spacecraft validations—while maintaining a similar latitudinal extent.

3.2. Comparison with the spherical (cone) model in the heliosphere

Next, we explore how the differences at the model inner boundary of 0.1 au translate in the heliospheric domain. Figure 4 shows the radial speed in the ecliptic and meridional planes for the sphere (cone) and spheroid CMEs. The results in the two runs appear rather similar in the meridional plane, where the two CMEs are initiated with a difference of only 5° (~2 R_s) in their angular extent. On the other hand, the spheroid CME is visibly wider in the equatorial plane, which coincides with the direction of its major axis. Although the CME nose is located at a similar heliocentric distance for

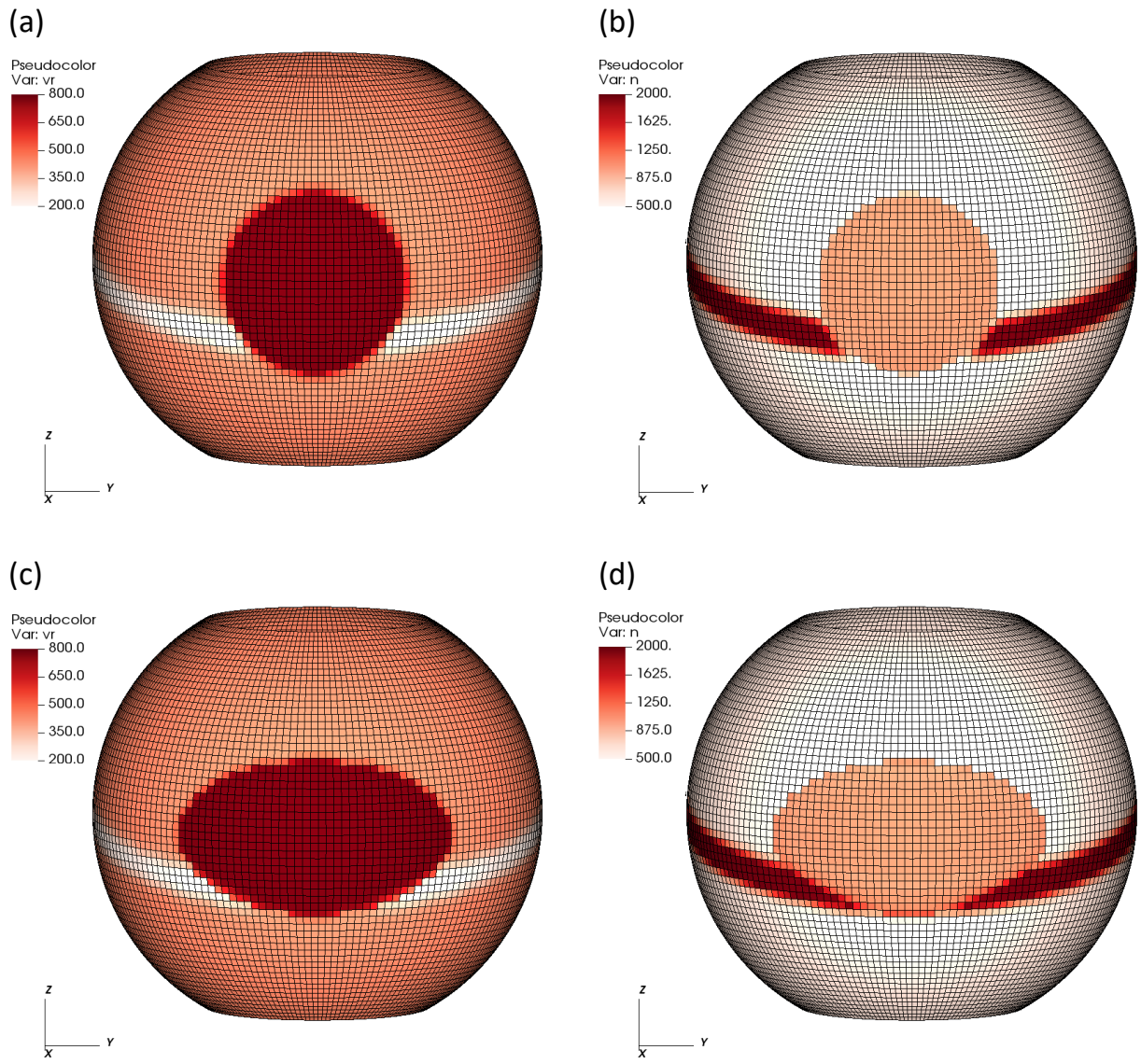

Fig. 3. 3-D views of the radial velocity (v_r, in units of km s^{-1}) and number density (n, in units of cm^{-3}) at the heliospheric inner boundary during the CME insertion, for the two simulations performed. (a): v_r for the cone (spherical) CME model. (b): n for the cone (spherical) CME model. (c): v_r for the spheroidal CME model. (d): n for the spheroidal CME model. The area where the CME is being inserted (v_r = 800 km s^{-1}, n = 600 cm^{-3}) is visible as the red (orange) patch on the left (right).

both simulations at the time of the snapshot shown in Figure 4 (suggesting a similar arrival time at 1 au, see Section 3.3), it is clear that the spheroid CME appears approximately 20° wider than the cone one—note that the green lines in panels (a) and (c) mark increments of 10° in longitude from the fictitious Sun–Earth line, located at (θ, ϕ) = (0°, 0°).

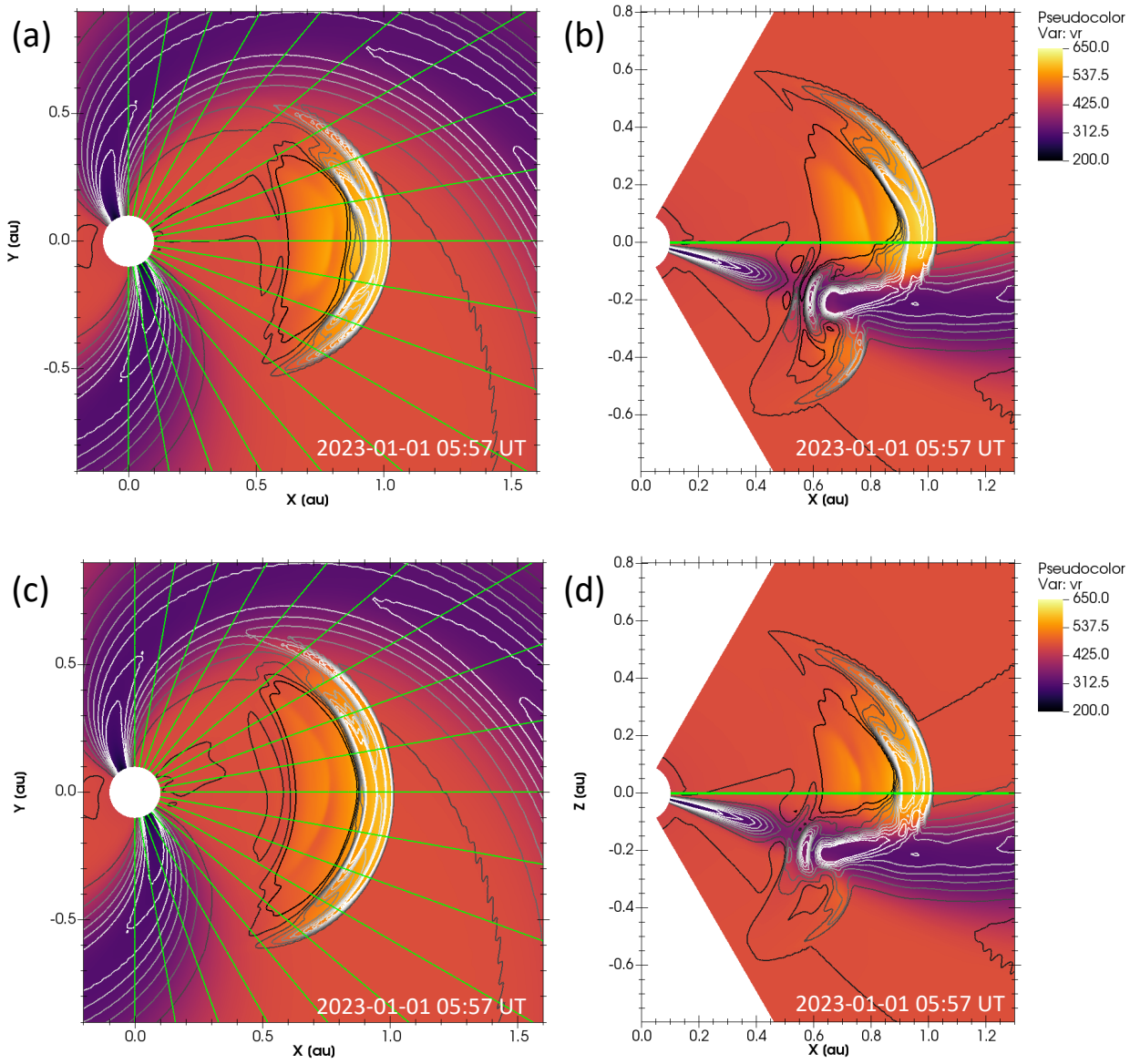

Fig. 4. Modeling results for the fictitious CME with the sphere and spheroidal CME models. The panels show the radial speed v_r in the equatorial (left) and meridional (right) plane on 2023-01-01 05:57 UT, when the CME nose was close to 1 au in both simulations. Representative scaled number density nr^2 values are indicated by the gray contour lines. (a–b): spherical (cone) CME model. (c–d): spheroidal CME model. The green lines marks directions to representative virtual spacecraft located at $\theta = 0°$ and ϕ between $-90°$ and $90°$, with $10°$ increments.

3.3. Comparison with the spherical (cone) model at 1 au

Figure 5 shows the spherical (cone) and spheroidal run time series for the radial speed and number density at 1 au at the CME nose (θ, ϕ) = (0°, 0°) and as a function of the impact parameter (from the center to the flanks, with virtual spacecraft placed at 10° separation). Locations are shown at longitudes of 0° (a), 10° (b), 20° (c), 30° (d), 40° (e), and 50° (f) on the western CME flank.

We identify the CME arrival time at each location and for each run by comparing the CME time series with a time series obtained from running the sole solar wind without any CME inserted, and by identifying the first time the two time series diverge in terms of their speed and/or density parameters. The resulting CME arrival times at each location are marked by vertical lines in Figure 5. Comparable results are found at the spacecraft locations on the eastern CME flank (not shown). Even from a visual inspection of the results, we can appreciate how the difference in the CME arrival time increases with the longitudinal offset from the CME longitudinal direction of propagation (initiated at $\phi = 0°$).

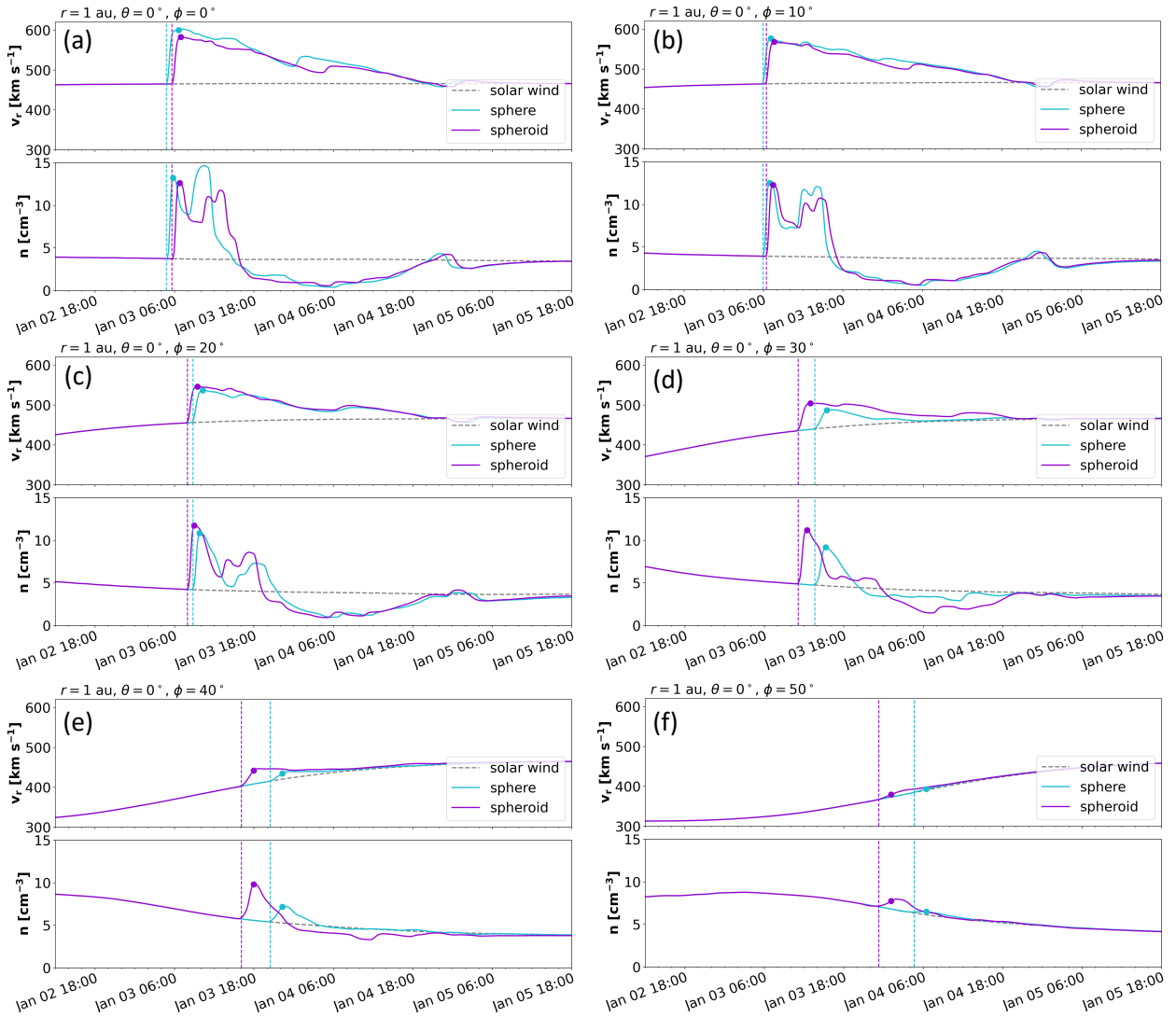

Fig. 5. Radial speed and number density recorded by virtual spacecraft at 1 au for the cone (teal) and spheroid (violet) CME models. As a reference, the ambient solar wind values are plotted in gray. Locations are shown at ϕ values of (a) 0°, (b) 10°, (c) 20°, (d) 30°, (e) 40°, and (f) 50°. Vertical dashed lines mark the CME arrival time in the two runs. Dots mark the CME impact (peak) speed and density.

In Figure 6, we further quantify this longitudinal effect for the CME arrival time, impact speed, and impact density. Panel (a) reports the time difference in the CME arrival time between the two

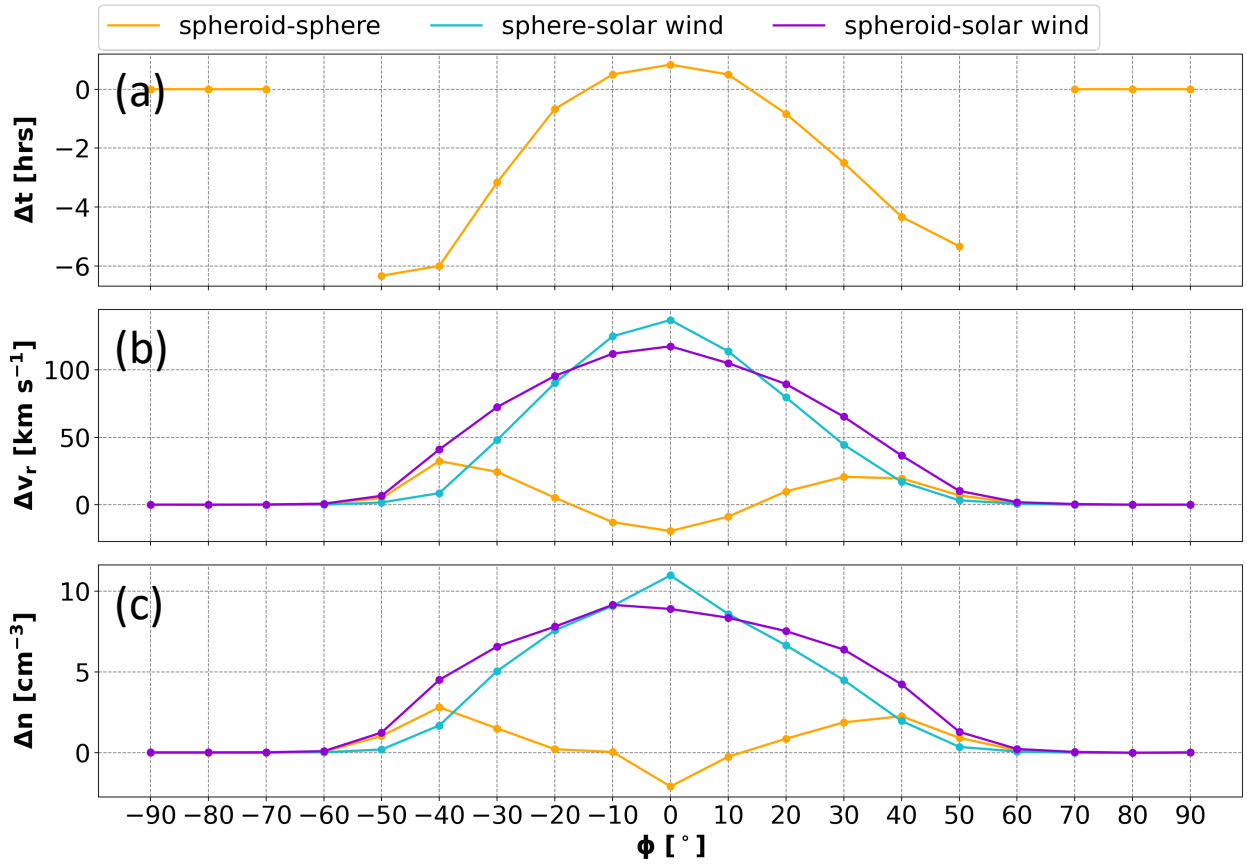

Fig. 6. Difference between the spheroid and sphere (cone) CME impact properties at 1 au, as a function of the spacecraft longitude. (a): difference in the CME arrival time. (b): difference in the CME impact (peak) speed. (c): difference in the CME impact (peak) density. The orange lines are calculated by subtracting the sphere to the spheroid properties. The teal (violet) lines show the subtracted values between the sphere (spheroid) and the ambient solar wind.

simulations, calculated as $\Delta t = t_{\rm spheroid} - t_{\rm sphere}$. We observe that while at $\phi = \phi_{\rm CME} = 0°$ the CMEs in the two runs arrive within ∼1 hour from each other, the larger the longitudinal offset, the more the CME in the cone model lags behind the spheroidal CME. This delay reaches a maximum of ∼5–6 hours at $\phi = \pm 50°$, and is consistent with the broader front of the spheroidal CME (due to its larger width) in the equatorial plane compared to the cone CME. Conversely, the cone CME is characterized by a more convex front due to its spherical, narrower geometry. Furthermore, spacecraft located at $\phi = \pm 60°$ only detect the passage of the CME with spheroidal geometry (corresponding to the missing points in Figure 6 (a)). Spacecraft located at larger longitudinal separations from the CME direction of propagation do not detect the CME in either of the two simulations (corresponding to the zero values in Figure 6(a)). It is important to note that although the values for Δt reported for this specific case are smaller than the current prediction capability for the CME arrival time (estimated to be around ±10 hours; Riley et al., 2018; Vourlidas et al., 2019), our results demonstrate

how effects related to the CME geometry are contributing to the overall arrival time prediction uncertainty unless the CME geometry is not properly accounted for. Furthermore, Δt may be larger, possibly exceeding ±10 hours, for other combinations of CME and solar wind parameters: in such a case, these differences would become comparable to (if not greater than) prediction uncertainties, thus directly affecting the prediction capabilities for given CME events. These results also demonstrate how the choice of CME geometry not only affects predictions of the CME arrival time, but also predictions of the CME hit/miss at a given spacecraft location.

Figure 6(b) and (c) show the results for the difference in the impact (i.e. peak) CME speed and density, calculated as $\Delta v_r = v_{r,\mathrm{spheroid}} - v_{r,\mathrm{sphere}}$ and $\Delta n = n_{\mathrm{spheroid}} - n_{\mathrm{sphere}}$. Spacecraft within $\phi = \pm 10°$ correspond to the locations where the cone CME arrives slightly earlier ($\Delta t > 0$) and faster ($\Delta v < 0$) than the spheroid CME. In this region, the cone CME is also denser ($\Delta n < 0$). Conversely, spacecraft at $20° \leq |\phi| \leq 50°$ show the spheroidal CME arriving earlier ($\Delta t < 0$), faster ($\Delta v > 0$), and denser ($\Delta n > 0$) than the cone one, consistently with its broader front. Overall, Δv ranges from -20 km s^{-1} at $\phi = 0°$, to 32 (20) km s^{-1} at $\phi = -40°(+40°)$, while Δn goes from -2 cm^{-3} at $\phi = 0°$, to 3 (2) cm^{-3} at $\phi = -40°(+40°)$. While these Δv and Δn values are somehow moderate when considered individually, they are expected to have a cumulative effect in the level of perturbation induced on geospace. We explore this aspect in Section 3.4 by estimating the level of CME geoeffectiveness hypothetically expected at each synthetic spacecraft location (each representing the location of a fictitious Earth) in terms of induced magnetospheric compression and geomagnetic storm strength.

3.4. Comparison with the spherical (cone) model: prediction of CME geoeffectiveness

To conclude our analysis of fictitious CME events, we want quantify the potential impact of different CME shapes on the space weather predictions at 1 au. To do so, we follow the approach by Scolini et al. (2018b) and use EUHFORIA simulation outputs at various virtual spacecraft at 1 au to compute: (1) the minimum magnetopause stand-off distance (dso) in the subsolar direction, based on the Shue model (Shue et al., 1997); and (2) the maximum Kp index, proxy of the CME-driven geomagnetic activity, by means of the coupling function proposed by Newell et al. (2008). The choice of these two metrics is based on the consideration that these are mainly susceptible to the CME dynamic pressure at impact, rather than to its internal magnetic structure (which is not realistically modeled in the simulations considered here). Furthemore, both official forecasts (e.g. from NOAA Space Weather Prediction Center, https://www.swpc.noaa.gov/products/3-day-forecast) and research-oriented forecasts (e.g. in the NASA Community Coordinated Modeling Center DONKI catalog, https://ccmc.gsfc.nasa.gov/tools/DONKI) are based on predictions from solar wind–Kp coupling functions, which makes the predicted Kp a standard metric for this sort of validation efforts. Despite the limitations common to such coupling functions (e.g. Luo et al., 2017; Lockwood, 2022), the use of the specific solar wind–Kp coupling function by Newell et al. (2008) also has the advantage to enable back-comparison with previous works on the validation of the EUHFORIA cone model (e.g. Scolini et al., 2018b,a). We calculate the predicted minimum dso and maximum Kp index based on EUHFORIA in situ time series for the full array of virtual spacecraft located at $\theta = 0°$ and evenly spanned from $\phi = -90°$ to $\phi = 90°$.

Figure 7 compares the predictions obtained from EUHFORIA time series at different virtual spacecraft for the two CME models. Both the minimum magnetopause stand-off distance and the maximum Kp index significantly depend on the impact location and CME model used. Figure 7(a)

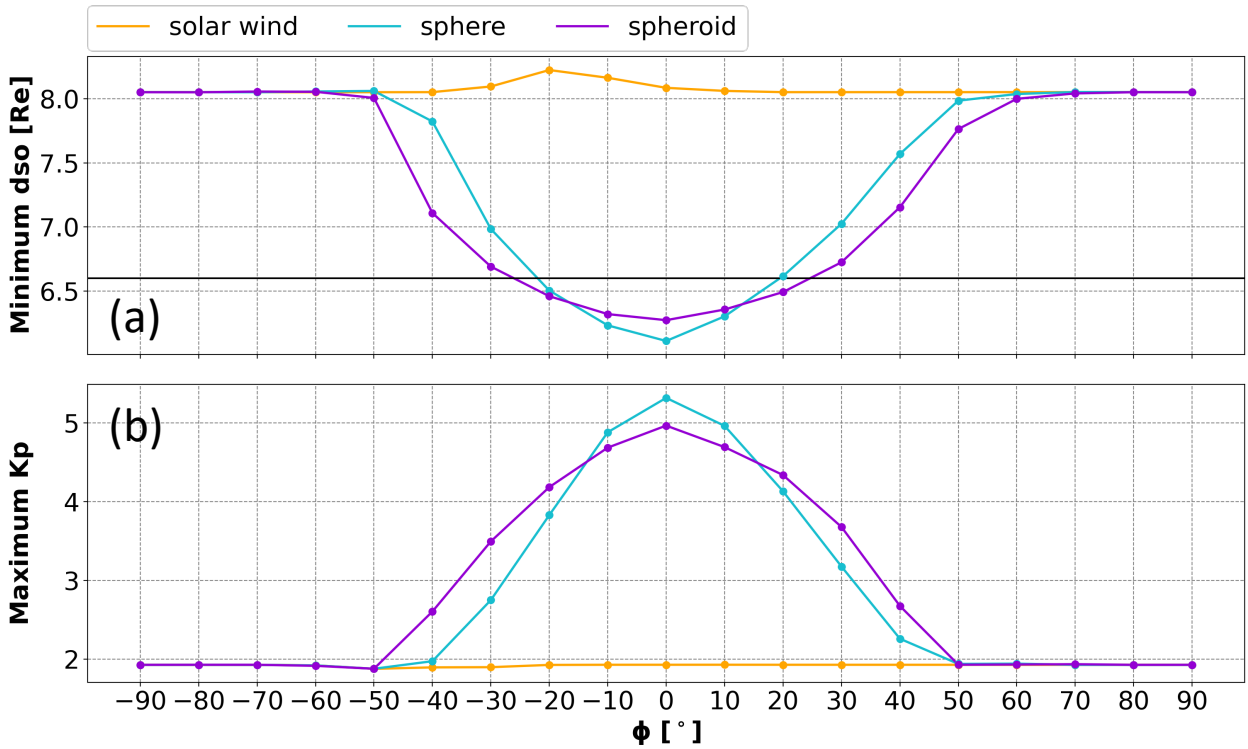

Fig. 7. CME geoeffectiveness prediction as a function of the spacecraft longitude. (a): estimate of the minimum magnetopause stand-off distance calculated using the model by Shue et al. (1997). The black horizontal line marks the geosynchronous orbits at 6.6 R_e. (b): estimate of the maximum Kp index calculated using the relation by Newell et al. (2008).

shows that the minimum magnetopause stand-off distance is moderately affected by the different CME models tested. The predicted minimum magnetopause stand-off distance is expected at $\phi = 0°$ in both models, where it reaches altitudes of 6.1 earth radii (R_e) and 6.3 R_e for the cone and spheroidal models, respectively. Figure 7(a) also shows that the choice of CME model influences whether and at which locations the magnetopause would be expected to cross the geosynchronous orbits (located at an altitude of 6.6 R_e), thereby significantly affecting the prediction of the expected CME impact on technological systems in space. In our simulations, the spacecraft locations where predictions are most uncertain with respect to whether the magnetopause will cross or not the geosynchronous orbits (meaning the cone and spheroidal model do not agree in their prediction) are those located at $|\phi|$ values between 20° and 30°. All locations at $|\phi| \leq 20°$ are predicted to have the magnetopause pushed below geosynchronous orbits, while all locations at $|\phi| \geq 30°$ are predicted to have the magnetopause remaining above geosynchronous orbits. The maximum difference in the predicted minimum magnetopause stand-off distance between the cone and spheroidal model is of 0.7 R_e at $\phi = -40°$, confirming predictions related to the impact of CME flanks are those most susceptible to the particular CME model used.

Figure 7(b) shows the results for the predicted maximum Kp index as function of the impact location and CME model used. The maximum Kp values predicted are 5.3 and 5.0 (corresponding to a minor storm level according to the National Oceanic and Atmospheric Administration (NOAA)

Geomagnetic Storm Scale classification[1]) in the cone and spheroidal model, respectively. Such values are expected at $\phi = 0°$. At larger $|\phi|$ values the predicted maximum Kp ranges between 4.9 and 1.9, corresponding to quiet-time levels. The maximum difference in the predicted maximum Kp between the two models is of 0.74 and is achieved at $\phi = -30°$, showing that, just as for the magnetopause stand-off distance, predictions at locations impacted by the CME flank are those most affected by the specific CME model used.

We conclude by noting that, as both models employed in this work model CMEs as non-magnetized plasma clouds inserted in the heliosphere without an internal magnetic field structure, the magnetic field is generally significantly underestimated compared to observations. Therefore, such estimates may provide just a lower limit for the CME geoeffectiveness, and the impact that a realistic magnetic field (e.g., obtained using a flux rope CME model) would have on the variation of the Kp index predictions cannot be assessed. However, prediction centers (e.g., the NOAA/Space Weather Prediction Centre and the UK MET office) still employ cone CME models to produce daily predictions of the space weather condition near Earth. Also, Kp forecasts formulated by employing cone CME models and empirical relations—similar to the one used in this work—are still widely used to validate model performances for both scientific and operational purposes (see, e.g., Mays et al., 2015). Therefore, we regard the discussion presented here as relevant given the current operational status and recent research publications.

4. Case study CME on 7 January 2014

In the following, we test the spheroidal CME model in EUHFORIA against a real CME event. As a case study, we choose the CME observed on 7 January 2014 and previously analyzed and modeled by Mays et al. (2015) using a tilted ellipsoid CME shape in the WSA–ENLIL+Cone model (e.g., Odstrcil et al., 2004).

Figure 1 shows the CME in the solar corona as seen by SOHO (representing the Earth viewpoint), STEREO-A, and STEREO-B (top row), and fitted with the cone (middle row) and croissant (bottom row) models. Both sets of reconstructions were performed using the GCS model and fitting tool, with the difference that for the cone case the so-called half-width parameter (quantifying the half-angular separation between the CME legs) was set to zero.

We use the results from the GCS reconstructions shown in Figure 1 to construct a set of input parameters for the CME in both the cone and spheroid CME models as described in Section 2. The resulting set of CME input parameters used in EUHFORIA is provided in Table 2. While the values for latitude, longitude, and tilt are direct outputs of the GCS reconstruction, the angular width parameters are obtained from the GCS-specific half-width and aspect ratio (i.e., the ratio of the CME size at two orthogonal directions) using the formulation outlined by Palmerio et al. (2023, Appendix A). The CME speed is estimated by fitting the CME with the GCS model in two successive time frames (on 7 January 2014 at ~19:10 and ~19:40 UT) and by considering the corresponding heliocentric distance traveled by the CME apex (or nose). The CME time of crossing through the model inner boundary is determined by linearly extrapolating the obtained CME kinematics to the 21.5 R_s (0.1 au) boundary height. The ratio of the CME major radius to the minor radius corresponds to a spheroid aspect ratio of 2. This set of GCS-based CME input

[1] http://www.swpc.noaa.gov/noaa-scales-explanation

	Spherical (cone) model	Spheroidal model
t_{CME}	2014-01-07 20:22 UT	2014-01-07 20:22 UT
ϕ_{CME}	36°	36°
θ_{CME}	−26°	−26°
v_{CME}	1910 km s^{-1}	1910 km s^{-1}
γ_{CME}	–	37°
$\omega_{\mathrm{CME}}/2$	44° (20.7 R_s)	–
r_{maj}	–	49° (24.7 R_s)
r_{min}	–	30° (12.4 R_s)
ρ_{CME}	1.5×10^{-18} kg m^{-3}	1.5×10^{-18} kg m^{-3}
T_{CME}	0.8×10^{6} K	0.8×10^{6} K
V_{CME}	1.26×10^{31} m^3	5.38×10^{30} m^3
m_{CME}	1.89×10^{13} kg	8.06×10^{12} kg
$E_{kin,\mathrm{CME}}$	6.06×10^{24} J	2.58×10^{24} J

Table 2. Input parameters used to model the 7 January 2014 CME with the cone and spheroidal models.

parameters for EUHFORIA are consistent with those reconstructed by Mays et al. (2015) for the same event. Similarly to Table 1, the bottom portion of Table 2 lists derived parameters such as the CME total volume (V_{CME}), mass (m_{CME}), and kinetic energy ($E_{\mathrm{kin,CME}}$) in the two cases. In contrast to the fictitious event discussed in Section 3, however, the values for the spheroidal model in this event are 57% smaller than for the spherical (cone) model. Since each of these parameters likely has an influence on the global propagation of the CME front, we expect them to also impact the arrival time/speed of the CME and the resulting geo-effectiveness at a specific target location such as Earth (the latter one mainly due to the different dynamic pressure in the two EUHFORIA runs). We further discuss these aspects below.

To model the ambient solar wind, we drive the EUHFORIA coronal model using a single National Solar Observatory Global/Oscillation Network Group (NSO/GONG; Harvey et al., 1996) daily-updated standard synoptic magnetogram taken on 7 January 2014 at 01:04 UT. The coronal model set up used is the same as in Pomoell and Poedts (2018). Simulations are performed over a computational domain extending from 0.1 au to 2 au in the radial (r) direction, and covering ±60° in the latitudinal (θ) direction and ±180° in the longitudinal (ϕ) direction. We employ a uniform grid with 256 cells in the radial direction and a resolution of 4° in the latitudinal and longitudinal directions.

It is important to note that both uncertainties in the solar wind and CME parameters can have significant effects on the predicted propagation and impact of CMEs at given target locations. For example, Riley and Ben-Nun (2021) explored the sources of uncertainty in the predicted CME arrival time at Earth using a set of numerical MHD simulations of cone CMEs in different ambient solar wind backgrounds. They found that uncertainties in each of the CME initial parameters, such as longitude, latitude, width, and speed, introduce between 2.5 and 7.5 hours of uncertainty into the predicted CME arrival time at Earth. Furthermore, they concluded that the ambient solar wind structure was the largest source of such an uncertainty, and that without better constraints on the initial conditions of heliospheric simulations (i.e. from coronal models), it is likely that the CME arrival time error will remain close to ±10 hours (Riley et al., 2018). Even more so, Ledvina et al.

(2023) found that input photospheric (i.e., magnetogram maps) and coronal (i.e., magnetic field reconstructions) conditions in modeling CME propagation can have a profound effect on the structures predicted in situ even in the case of a simplified, uniform background solar wind. At the same time, the choice of CME input parameters has a direct effect on the resulting propagation and estimated impact(s). It has been shown that, even when employing a single propagation model and keeping the background solar wind conditions unchanged, CME properties derived from coronagraphic reconstructions performed by different users, or even by the same user assuming different CME morphologies, can result in CME predictions that vary significantly in timing and severity (Palmerio et al., 2022). Overall, it has been demonstrated that CME reconstructions performed independently may be expected to differ by 4.0° in the latitude, 8.0° in the longitude, 24.0° in the tilt, 9.3° in the angular width, and 115 km s^{-1} in the speed (Kay and Palmerio, 2024). In the context of the GCS model employed here, a sensitivity analysis performed by Thernisien et al. (2009) and a multi-user investigation conducted by Verbeke et al. (2023) reported typical uncertainties of a few degrees in the latitude and longitude (the former being slightly better constrained), ∼20° in the tilt, ∼10° in the half-width, and ∼0.5 R_S in the nose height. Such uncertainties are also compatible with those reported in Table 1 by Mays et al. (2015) for the specific CME considered here (i.e. the 7 January 2014 event), based on the GCS as well as other reconstruction methods. For this specific event, a typical ∼10° uncertainty in the half-width derived from the GCS reconstruction also implies the two shapes employed in the cone (spherical) and spheroidal EUHFORIA runs are clearly distinct from each other given their half-widths differ for more than the typical uncertainty, at least along the CME minor axis direction. More generally, Kay and Nieves-Chinchilla (2021) studied the sensitivity of CME input parameters in the framework of analytical modeling, and found that different properties tend to be more important in the cases of CMEs with different speeds, the most critical parameters being generally the mass, magnetic field strength, adiabatic index, and axial field profile. Hence, we caution against drawing strong conclusions from the results presented in this section, especially in light of the relatively large uncertainties involved in modeling the different domains of the Sun–Earth (or Sun–heliosphere) chain.

4.1. Comparison of CME models at 0.1 au

Figure 8 shows the modeling results on the spherical surface at r = 0.1 au on 7 January 2014 around 22:00 UT, just after the CME insertion in the heliospheric domain. The figure demonstrates the difference in the CME front shape between the two runs, with the cone CME being more extended than the spheroid one. In the phases immediately after their insertion in the heliosphere, both CMEs are propagating tangentially to the Sun–Earth direction.

We note that, in contrast to the fictitious CME case (see Figure 3), for this event the cross-section of the spheroidal CME intersects the solar equatorial plane significantly less than the spherical one. Even more so, while the cone CME crosses Earth's projected position with its northeastern edge, the spheroid does not feature a component along the Sun–Earth line at 0.1 au. Nevertheless, an encounter at Earth may still take place due to processes such as CME expansion in the heliosphere and interactions with the structured solar wind (see, e.g., the reviews of Manchester et al., 2017; Luhmann et al., 2020, on the interplanetary evolution of CMEs).

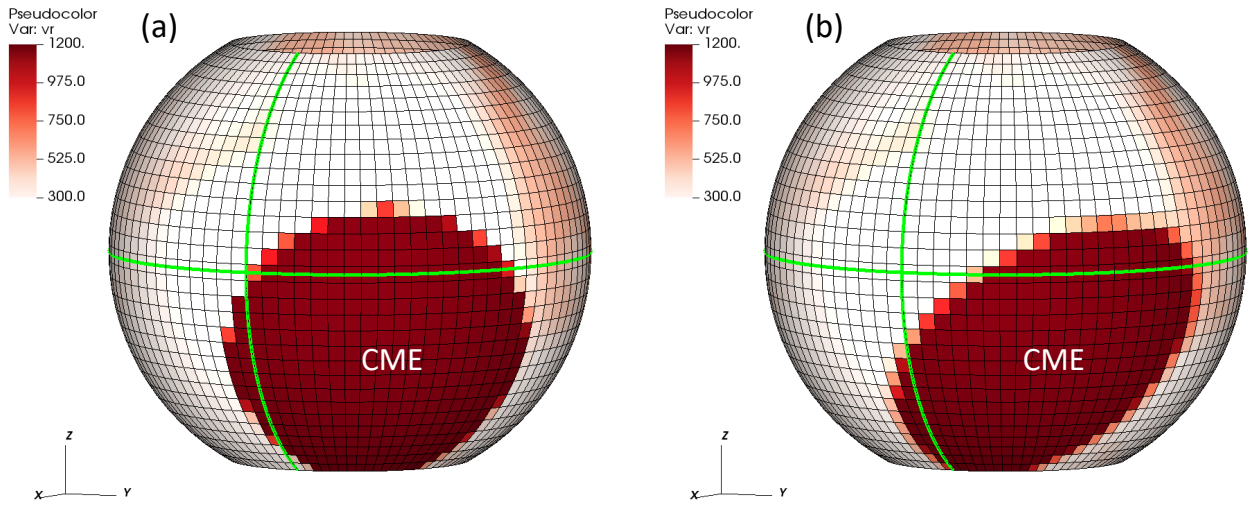

Fig. 8. 3-D views of the radial velocity (v_r, in units of km s^{-1}) at r = 0.1 au on 7 January 2014 around 22:00 UT (during the CME insertion), for the two simulations performed. (a): cone. (b): spheroid. The green lines mark the central meridian and the solar equator. The area where the CME is being inserted is visible as a red patch is the southwestern quadrant.

4.2. Comparison of CME models in the heliosphere

Figure 9 shows the modeling results in the equatorial and meridional planes around 07:00 UT on 9 January 2014, when the CME nose was close to 1 au in the two simulations. The figure shows that the cone CME is generally more extended and faster than the spheroid CME in both the ecliptic plane (panels (a) and (c)) and in the meridional one (panels (b) and (d)) at this stage of propagation. While close to the CME nose this is most likely caused by the higher mass of the cone CME compared to the spheroidal CME, the differences near the CME flanks are primarily due to the different geometry employed in the two runs. Furthermore, contrarily to the situation depicted in Figure 8 at the model inner boundary, both runs show that the CME has a propagation component along the Sun–Earth direction, most likely due to the expansion of its shock front during the initial propagation phases in the heliospheric domain.

4.3. Comparison of CME models at Earth

Figure 10 compares the EUHFORIA time series at Earth in the two simulations with real observations from the Wind (Ogilvie and Desch, 1997) spacecraft, specifically from the Solar Wind Experiment (SWE; Ogilvie et al., 1995) instrument.

The CME is observed to arrive at Wind on 9 January at 19:40 UT, when its interplanetary shock was detected (from the IPshocks database[2]; Kilpua et al., 2015). The shock was followed by a sheath region and by the CME ejecta, which started on January 10 at about 07:00 UT and ended on January 11 at about 03:00 UT as indicated by magnetic field rotations and the presence of bi-directional suprathermal electron flux (not shown). As shown in Figure 10, EUHFORIA modeled

[2] http://ipshocks.fi/database

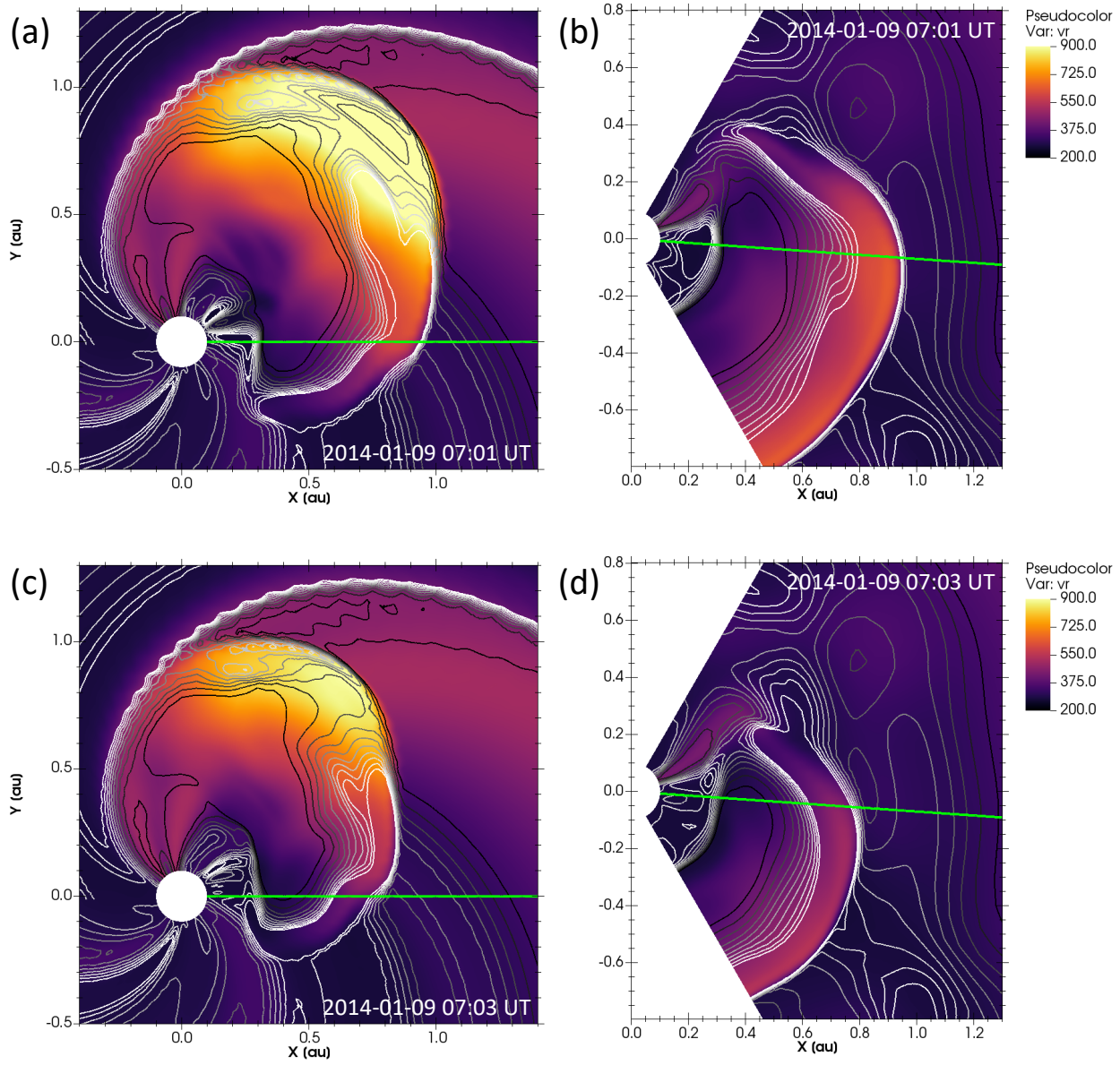

Fig. 9. Modeling results for the 7 January 2014 CME with the cone and spheroidal CME models on 9 January 2014 around 07:00 UT. The format is the same as Figure 4. The green lines mark the Sun–Earth direction.

the CME to arrive at Earth on 9 January at 07:41 UT using the spherical (cone) model, and on 9 January at 17:03 UT using the spheroidal model. Using the input parameters described above, the spheroidal model thus performs significantly better than the cone in predicting the CME arrival at Earth ($\Delta t_{\rm err} = t_{\rm predicted} - t_{\rm observed} = -11.97$ hours for the cone, compared to $\Delta t_{\rm err} = -2.6$ hours for the spheroid). Furthermore, we note that the relative difference in the arrival time between the two runs at Earth is of almost 10 hours, even though the two CMEs were launched with the same initial speed in the two simulations. This result clearly demonstrates how the choice of CME model can have an

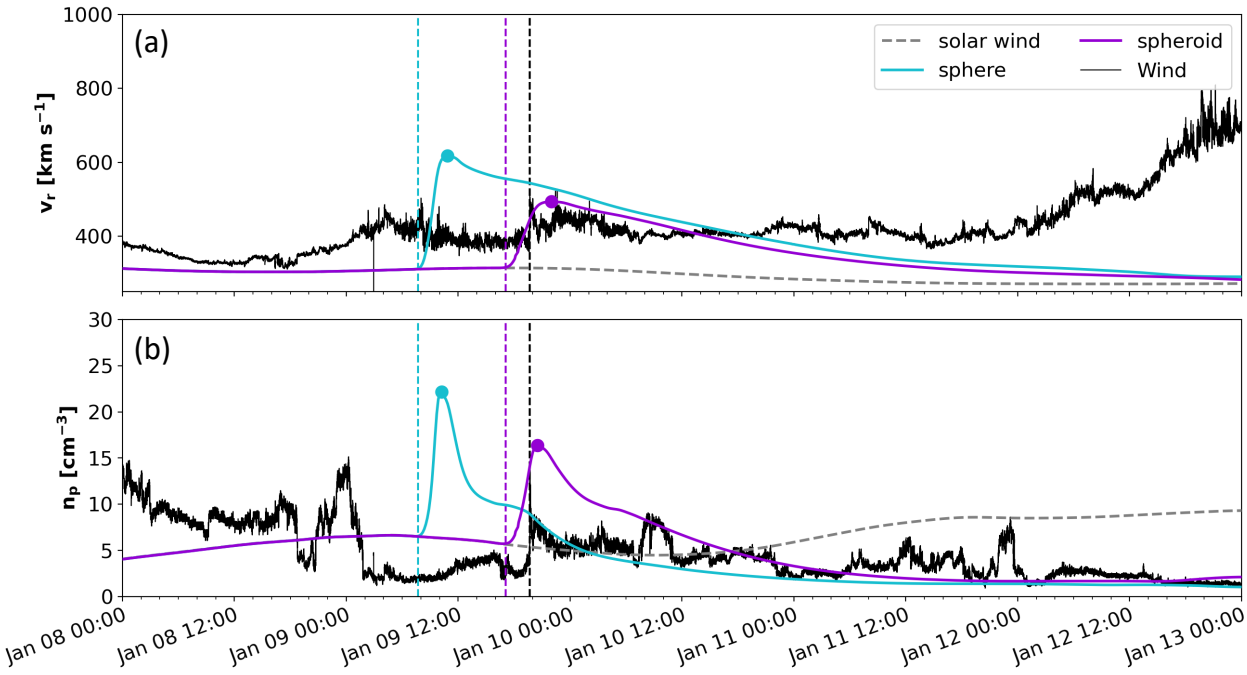

Fig. 10. EUHFORIA predictions at Earth for the 7 January 2014 CME. (a): radial speed. (b): proton number density. Cone and spheroidal model results are shown in teal and violet, respectively. As a reference, ambient solar wind model results are plotted in gray. Real measurements from Wind are shown in black. Vertical dashed lines mark the CME arrival time in the two EUHFORIA runs and in Wind observations. The CME impact speed and density in EUHFORIA runs is marked by the dots.

effect on CME arrival time predictions that is at least comparable to current prediction capabilities (estimated to be around ±10 hours; Riley et al., 2018; Vourlidas et al., 2019).

In Wind observations, the CME had an impact peak speed of about 480 km s^{-1} and a peak proton density of about 12 cm^{-3}. Figure 10 shows that the spherical (cone) model predicted a CME peak speed of 617 km s^{-1}, and a peak proton density of 22 cm^{-3}. These values are significantly larger than the observed values (about 140 km s^{-1} and 10 cm^{-3} for the impact speed and density, respectively). On the other hand, the spheroidal model was able to predict the CME impact speed and density remarkably well with respect to the observed values. In this case, the modeled CME peak speed was 494 km s^{-1}s, and the peak proton density was 16 cm^{-3}, which are only about 15 km s^{-1} and 4 cm^{-3} higher than observed. For comparison, Mays et al. (2015) report that the uncertainties in the CME initial parameters affect the CME arrival time at Earth by up to $+9/-7$ hours compared to the mean arrival time predicted by the WSA–ENLIL+Cone model. However, in their simulations the mean predicted arrival time was shifted by about 18 hours compared to the observed arrival time at Earth. Additionally, the CME impact speed and density were overpredicted by 100–700 km s^{-1} and by a factor 3–5 compared to the observed values, respectively. With respect to these metrics, the EUHFORIA spheroidal CME simulation presented in this work therefore performs significantly better. It is however important to emphasize that the spheroidal CME simulation performed in this work only represents a single realization: while we can expect similar uncertainties in the predic-

tions at Earth as those reported by Mays et al. (2015), more extensive ensemble simulations should be performed in order to determine the actual prediction performances for a broad set of ambient solar wind realizations and CME initial parameters.

Although it remains challenging to disentangle the effects of different CME geometries from that of different CME masses and kinetic energies, the latter are most likely dominant close to the CME nose, while geometrical effects are expected to be predominant close to the flanks (i.e. including at Earth location). We caution that future targeted validation efforts are required to precisely pinpoint the magnitude and localization of these effects across CME fronts, for different combinations of CME and solar wind parameters.

4.4. Comparison of CME models: prediction of CME geoeffectiveness

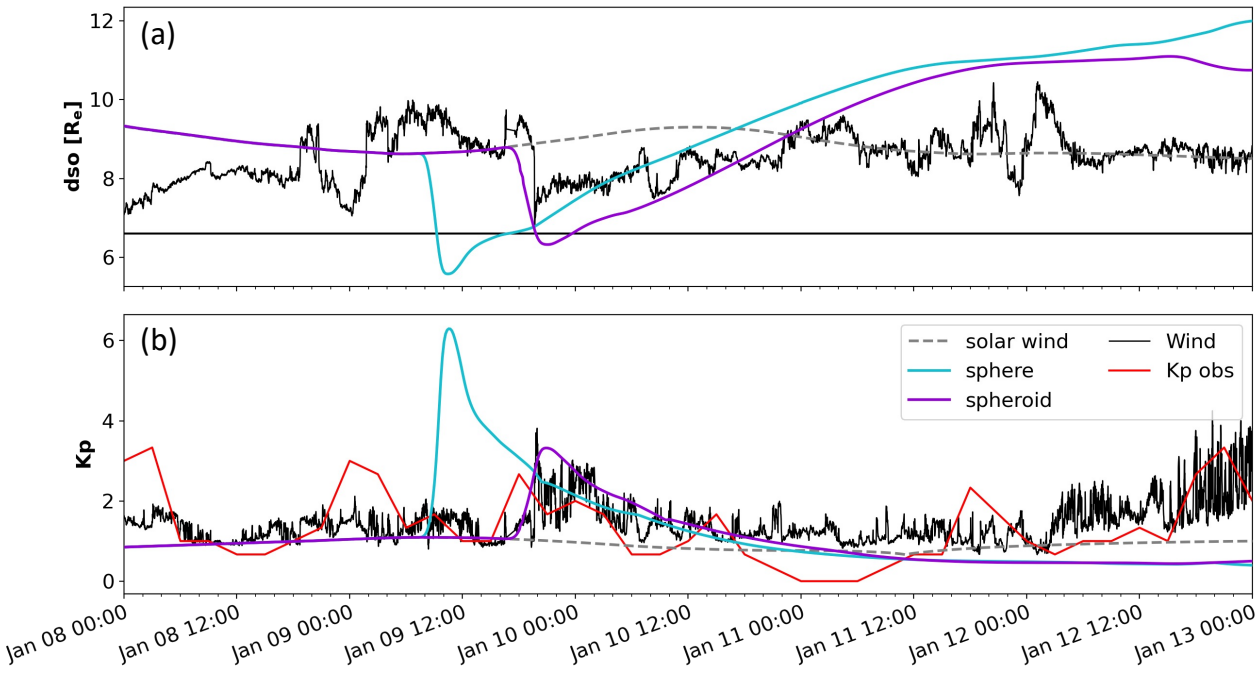

Fig. 11. Modeled and observed CME geoeffectiveness as a function of time. (a): magnetopause stand-off distance calculated from EUHFORIA and Wind time series using the model by Shue et al. (1997). The black horizontal line marks the geosynchronous orbits at 6.6 R_e. Cone and spheroidal model results are shown in teal and violet, respectively. As a reference, ambient solar wind model results are plotted in gray. Estimates from Wind measurements are shown in black. (b): Kp index calculated from EUHFORIA and Wind time series using the relation by Newell et al. (2008). 3-hour Kp measurements are shown in red.

As final step, we compute the predicted CME geoeffectiveness (in terms of magnetopause compression and Kp index, as in Section 3.4) based on EUHFORIA time series at Earth for both the cone (spherical) and spheroidal simulations, and we compare them with predictions obtained from

Wind time series, as well as with actual measurements of the Kp index (from the GFZ – Helmholtz Center Potsdam[3]) at 3-hour cadence. Results are shown in Figure 11.

In terms of the CME-induced compression of the Earth's magnetopause (panel (a)), the cone simulation predicts the dso to reach a minimum value of about 5.6 R_e, while the spheroid simulation predicts it to only reach a minimum of 6.3 R_e. Both predictions are below geosynchronous orbits, thus in this case, the two EUHFORIA simulations agree in predicting that satellites in geosynchronous orbits may become exposed to solar wind conditions during the CME impact. However, the time evolution of the dso predicted by the two simulations is quite different, as expected from the different CME arrival times and impact parameters predicted. The spheroidal model, in particular, is the one that matches better with dso predictions based on Wind data. This is true both for the dso temporal evolution, as well as for the predicted minimum dso (6.6 R_e based on Wind data, compared to 6.3 R_e from the spheroidal EUHFORIA simulation).

The two EUHFORIA simulations also predict significantly different space weather impacts in terms of geomagnetic storm strength based on the Kp index (panel (b)). The cone simulation predicts a maximum Kp of 6.3 (corresponding to a moderate storm according to NOAA levels), while the spheroidal simulation predicts a maximum Kp of only 3.3 (corresponding to a quiet state). For comparison, the Wind time series predicts a maximum Kp around 3.9, and the observed maximum Kp associated with the event was classified as 3− (corresponding to quiet conditions) by NOAA. As predictions from the cone model result in a dramatic overestimation of the CME geoeffectiveness for this particular event, this case clearly demonstrates how an appropriate choice of CME model in heliospheric simulations can provide a significant improvement to the predicted CME geoeffectiveness based on the Kp index. Finally, we note that the measured Kp for this specific event is very well reproduced by applying the solar wind–coupling function by Newell et al. (2008) empirical relation to Wind time series. This gives us additional confidence that this empirical relation, despite dating back more than a decade, is doing a rather good job in capturing the main coupling between the solar wind and geomagnetic response in terms of the Kp for this specific event.

Ultimately disentangling the impact of different CME geometries from that of different CME masses and kinetic energies on the resulting geoeffectiveness remains challenging without performing ad-hoc, extensive validation studies. However, we note here as well that differences in the CME masses and kinetic energies are most likely dominant close to the CME nose, while geometrical effects are expected to be predominant close to the flanks (i.e. including Earth's location).

5. Conclusions

In this paper, we have described the implementation and initial validation of the spheroid CME model in the 3-D MHD EUHFORIA code. After presenting the mathematical description of the spheroidal structure, we have shown a comparison of EUHFORIA simulation runs employing the traditional cone (spherical) ejecta and the newly-implemented spheroidal one for an idealized CME, as well as for an event that erupted on 7 January 2014 and that was later observed at Earth as a flank encounter. We have demonstrated that, at least under the specific conditions considered here, the new spheroidal implementation provided an improvement compared to the traditional cone model.

[3] ftp://ftp.gfz-potsdam.de/pub/home/obs/kp-ap/

In the first validation experiment (i.e., the one with fictitious CMEs), we have found that differences in CME arrival time and speed between the two models become more prominent with increasing distance from the CME nose. As a result, the expected CME geoeffectiveness (evaluated in terms of the Kp index and magnetopause stand-off distance) estimated from the two models' results at 1 au also becomes more different as the distance from the CME nose increases. Furthermore, we have demonstrated the choice of CME geometry not only affects predictions of the CME arrival time and impact properties, but can also impact the predictions of the CME hit/miss at spacecraft impacted by the CME flank extremities. Since the fictitious CME modeled represents an average fast CME in terms of speed and angular width, despite the idealised numerical set-up employed, one can expect the results to apply to a potentially large set of real CME events.

In the second validation test (i.e., the one with the real CME), we have found that a spheroidal CME structure is able to reproduce a better arrival time and speed of the observed flank encounter at Earth over the cone ejecta. Specifically, we noted that the CME arrival time and speed differed by ∼10 hours and ∼120 km s^{-1}, respectively, for the two CMEs that were launched with the same velocity, mass density, and temperature, and only differed for the morphology of their cross-section. The predicted geoeffectiveness was also highly affected by the choice of CME model. Particularly the prediction of the induced geomagnetic storm strength varied from a quiet state (Kp of 3 for the spheroid CME model, in remarkable agreement with actual Kp measurements at Earth) to a moderate storm (Kp above 6 for the cone CME model). This event thus clearly demonstrated how an appropriate description of the CME flanks in heliospheric simulations can provide a significant improvement to the predicted CME geoeffectiveness, particularly in the case flank encounters.

Although further investigations are needed in the future to quantify exactly in how many cases and to which extent the spheroidal model performs better than the cone model, the results presented in this work clearly demonstrate the potential of the new spheroid approach in providing improved space weather forecasts, particularly with respect to flank CME encounters. Employing a spheroidal CME morphology in 3-D MHD heliospheric simulations can constitute a significant improvement over the traditional cone model, while maintaining the physics and assumptions of the overall simulation—and, thus, the computational time—fairly unchanged. This is especially advantageous in the context of real-time space weather forecasts, where magnetized CMEs are currently not (yet) employed. We note that the WSA–ENLIL+Cone model, currently used for operations by several forecasting agencies, has also implemented a so-called ellipsoidal geometry for CMEs (as the one showcased in the work of Mays et al., 2015), which is however only employed in research applications at the time of writing (Odstrcil, 2023). One source of difficulty may be related to the adopted coronal reconstruction technique to derive CME input parameters (e.g., the "simpler" SWPC-CAT versus the "more complex" GCS). Nevertheless, it has been shown that CMEs can be relatively easily be fitted with ellipses in coronagraph imagery even when a single viewpoint is available (e.g., Yurchyshyn et al., 2007), and the method could be extended to two or more simultaneous observers without recurring to geometrical descriptions characterized by many free parameters. We also note that this work presents a first validation of the performance of the spheroid CME model versus the traditional cone CME model without considering the effect of the uncertainties affecting the determination of the initial CME parameters. Thus, while our results suggest this new CME implementation may perform better than the traditional cone model under specific conditions, and while a general improvement compared to the traditional cone model is also expected, whether this is indeed achieved remain to be proven in future studies.

In conclusion, a larger validation study to evaluate the advantages of employing a spheroidal versus a spherical CME model will provide more robust benchmarking, but the results presented in this work show that the spheroid approach is a promising avenue to pursue toward the improvement of current space weather forecasting capabilities.

Acknowledgements. EUHFORIA is developed as a joint effort between the University of Helsinki and KU Leuven. The simulations were carried out at the VSC–Flemish Supercomputer Center, funded by the Hercules foundation and the Flemish Government–Department EWI. EP acknowledges support from NASA's HTMS (grant no. 80NSSC20K1274) and LWS-SC (grant no. 80NSSC22K0893) programs as well as NSF's PREEVENTS (grant no. ICER-1854790) program.

References

Asvestari, E., J. Pomoell, E. Kilpua, S. Good, T. Chatzistergos, M. Temmer, E. Palmerio, S. Poedts, and J. Magdalenic, 2021. Modelling a multi-spacecraft coronal mass ejection encounter with EUHFORIA. *Astron. Astrophys.*, **652**, A27. 10.1051/0004-6361/202140315. 1

Cremades, H., and V. Bothmer, 2004. On the three-dimensional configuration of coronal mass ejections. *Astron. Astrophys.*, **422**, 307–322. 10.1051/0004-6361:20035776. 1

Fisher, R. R., and R. H. Munro, 1984. Coronal transient geometry. I - The flare-associated event of 1981 March 25. *Astrophys. J.*, **280**, 428–439. 10.1086/162009. 1

Gopalswamy, N., 2006. Coronal Mass Ejections of Solar Cycle 23. *J. Astrophys. Astron.*, **27**, 243–254. 10.1007/BF02702527. 3

Harvey, J. W., F. Hill, R. P. Hubbard, J. R. Kennedy, J. W. Leibacher, et al., 1996. The Global Oscillation Network Group (GONG) Project. *Science*, **272**(5266), 1284–1286. 10.1126/science.272.5266.1284. 4

Isavnin, A., 2016. FRiED: A Novel Three-dimensional Model of Coronal Mass Ejections. *Astrophys. J.*, **833**(2), 267. 10.3847/1538-4357/833/2/267. 1

Jang, S., Y. J. Moon, R. S. Kim, H. Lee, and K. S. Cho, 2016. Comparison between 2D and 3D Parameters of 306 Front-side Halo CMEs from 2009 to 2013. *Astrophys. J.*, **821**(2), 95. 10.3847/0004-637X/821/2/95. 3

Kataoka, R., T. Ebisuzaki, K. Kusano, D. Shiota, S. Inoue, T. T. Yamamoto, and M. Tokumaru, 2009. Three-dimensional MHD modeling of the solar wind structures associated with 13 December 2006 coronal mass ejection. *J. Geophys. Res.*, **114**(A10), A10102. 10.1029/2009JA014167. 1

Kay, C., and T. Nieves-Chinchilla, 2021. Modeling Interplanetary Expansion and Deformation of CMEs With ANTEATR PARADE: Relative Contribution of Different Forces. *J. Geophys. Res. Space Phys.*, **126**(5), 2020JA028911. 10.1029/2020JA028911. 4

Kay, C., and E. Palmerio, 2024. Collection, Collation, and Comparison of 3D Coronal CME Reconstructions. *Space Weather*, **22**(1), e2023SW003796. 10.1029/2023SW003796. 4

Kilpua, E. K. J., N. Lugaz, M. L. Mays, and M. Temmer, 2019. Forecasting the Structure and Orientation of Earthbound Coronal Mass Ejections. *Space Weather*, **17**(4), 498–526. 10.1029/2018SW001944. 1

568 Kilpua, E. K. J., E. Lumme, K. Andreeova, A. Isavnin, and H. E. J. Koskinen, 2015. Properties and drivers of
569 fast interplanetary shocks near the orbit of the Earth (1995-2013). *J. Geophys. Res. Space Phys.*, **120**(6),
570 4112–4125. 10.1002/2015JA021138. 4.3

571 Lamy, P. L., O. Floyd, B. Boclet, J. Wojak, H. Gilardy, and T. Barlyaeva, 2019. Coronal Mass Ejections over
572 Solar Cycles 23 and 24. *Space Sci. Rev.*, **215**(5), 39. 10.1007/s11214-019-0605-y. 3

573 Ledvina, V. E., E. Palmerio, C. Kay, N. Al-Haddad, and P. Riley, 2023. Modeling CME encounters at Parker
574 Solar Probe with OSPREI: Dependence on photospheric and coronal conditions. *Astron. Astrophys.*, **673**,
575 A96. 10.1051/0004-6361/202245445. 4

576 Lockwood, M., 2022. Solar Wind—Magnetosphere Coupling Functions: Pitfalls, Limitations, and
577 Applications. *Space Weather*, **20**(2), e2021SW002989. 10.1029/2021SW002989. 3.4

578 Luhmann, J. G., N. Gopalswamy, L. K. Jian, and N. Lugaz, 2020. ICME Evolution in the Inner Heliosphere.
579 *Sol. Phys.*, **295**(4), 61. 10.1007/s11207-020-01624-0. 4.1

580 Luo, B., S. Liu, and J. Gong, 2017. Two empirical models for short-term forecast of Kp. *Space Weather*,
581 **15**(3), 503–516. 10.1002/2016SW001585. 3.4

582 Maharana, A., A. Isavnin, C. Scolini, N. Wijsen, L. Rodriguez, M. Mierla, J. Magdalenić, and S. Poedts,
583 2022. Implementation and validation of the FRi3D flux rope model in EUHFORIA. *Adv. Space Res.*,
584 **70**(6), 1641–1662. 10.1016/j.asr.2022.05.056. 1

585 Manchester, W., E. K. J. Kilpua, Y. D. Liu, N. Lugaz, P. Riley, T. Török, and B. Vršnak, 2017. The Physical
586 Processes of CME/ICME Evolution. *Space Sci. Rev.*, **212**(3-4), 1159–1219. 10.1007/s11214-017-0394-0.
587 4.1

588 Mays, M. L., B. J. Thompson, L. K. Jian, R. C. Colaninno, D. Odstrcil, et al., 2015. Propagation of the 7
589 January 2014 CME and Resulting Geomagnetic Non-event. *Astrophys. J.*, **812**(2), 145. 10.1088/0004-
590 637X/812/2/145. 1, 3.4, 4, 4, 4.3, 5

591 Millward, G., D. Biesecker, V. Pizzo, and C. A. de Koning, 2013. An operational software tool for the
592 analysis of coronagraph images: Determining CME parameters for input into the WSA-Enlil heliospheric
593 model. *Space Weather*, **11**(2), 57–68. 10.1002/swe.20024. 1

594 Möstl, C., T. Rollett, R. A. Frahm, Y. D. Liu, D. M. Long, et al., 2015. Strong coronal channelling and inter-
595 planetary evolution of a solar storm up to Earth and Mars. *Nat. Commun.*, **6**, 7135. 10.1038/ncomms8135.
596 1

597 Newell, P. T., T. Sotirelis, K. Liou, and F. J. Rich, 2008. Pairs of solar wind-magnetosphere coupling func-
598 tions: Combining a merging term with a viscous term works best. *J. Geophys. Res.*, **113**(A4), A04218.
599 10.1029/2007JA012825. 3.4, 7, 11, 4.4

600 Odstrcil, D., 2003. Modeling 3-D solar wind structure. *Adv. Space Res.*, **32**(4), 497–506. 10.1016/S0273-
601 1177(03)00332-6. 1

602 Odstrcil, D., 2023. Heliospheric 3-D MHD ENLIL simulations of multi-CME and multi-spacecraft events.
603 *Front. Astron. Space Sci.*, **10**, 1226992. 10.3389/fspas.2023.1226992. 5

Odstrcil, D., P. Riley, and X. P. Zhao, 2004. Numerical simulation of the 12 May 1997 interplanetary CME event. *J. Geophys. Res.*, **109**(A2), A02116. 10.1029/2003JA010135. 4

Ogilvie, K. W., D. J. Chornay, R. J. Fritzenreiter, F. Hunsaker, J. Keller, et al., 1995. SWE, A Comprehensive Plasma Instrument for the Wind Spacecraft. *Space Sci. Rev.*, **71**(1-4), 55–77. 10.1007/BF00751326. 4.3

Ogilvie, K. W., and M. D. Desch, 1997. The wind spacecraft and its early scientific results. *Adv. Space Res.*, **20**, 559–568. 10.1016/S0273-1177(97)00439-0. 4.3

Palmerio, E., E. K. J. Kilpua, A. W. James, L. M. Green, J. Pomoell, A. Isavnin, and G. Valori, 2017. Determining the Intrinsic CME Flux Rope Type Using Remote-sensing Solar Disk Observations. *Sol. Phys.*, **292**(2), 39. 10.1007/s11207-017-1063-x. 1

Palmerio, E., C. O. Lee, M. L. Mays, J. G. Luhmann, D. Lario, et al., 2022. CMEs and SEPs During November-December 2020: A Challenge for Real-Time Space Weather Forecasting. *Space Weather*, **20**(5), e2021SW002993. 10.1029/2021SW002993. 4

Palmerio, E., A. Maharana, B. J. Lynch, C. Scolini, S. W. Good, J. Pomoell, A. Isavnin, and E. K. J. Kilpua, 2023. Modeling a Coronal Mass Ejection from an Extended Filament Channel. II. Interplanetary Propagation to 1 au. *Astrophys. J.*, **958**(1), 91. 10.3847/1538-4357/ad0229. 4

Palmerio, E., C. Scolini, D. Barnes, J. Magdalenić, M. J. West, et al., 2019. Multipoint Study of Successive Coronal Mass Ejections Driving Moderate Disturbances at 1 au. *Astrophys. J.*, **878**(1), 37. 10.3847/1538-4357/ab1850. 1

Pizzo, V., G. Millward, A. Parsons, D. Biesecker, S. Hill, and D. Odstrcil, 2011. Wang-Sheeley-Arge-Enlil Cone Model Transitions to Operations. *Space Weather*, **9**(3), 03004. 10.1029/2011SW000663. 1

Pomoell, J., and S. Poedts, 2018. EUHFORIA: European heliospheric forecasting information asset. *J. Space Weather Space Clim.*, **8**, A35. 10.1051/swsc/2018020. 1, 1, 2, 2, 4

Riley, P., and M. Ben-Nun, 2021. On the Sources and Sizes of Uncertainty in Predicting the Arrival Time of Interplanetary Coronal Mass Ejections Using Global MHD Models. *Space Weather*, **19**(6), e02775. 10.1029/2021SW002775. 4

Riley, P., M. L. Mays, J. Andries, T. Amerstorfer, D. Biesecker, et al., 2018. Forecasting the Arrival Time of Coronal Mass Ejections: Analysis of the CCMC CME Scoreboard. *Space Weather*, **16**(9), 1245–1260. 10.1029/2018SW001962. 3.3, 4, 4.3

Scolini, C., E. Chané, M. Temmer, E. K. J. Kilpua, K. Dissauer, et al., 2020. CME–CME Interactions as Sources of CME Geoeffectiveness: The Formation of the Complex Ejecta and Intense Geomagnetic Storm in 2017 Early September. *Astrophys. J. Suppl.*, **247**(1), 21. 10.3847/1538-4365/ab6216. 1

Scolini, C., M. Messerotti, S. Poedts, and L. Rodriguez, 2018a. Halo Coronal Mass Ejections during Solar Cycle 24: reconstruction of the global scenario and geoeffectiveness. *Journal of Space Weather and Space Climate*, **8**, A9. 10.1051/swsc/2017046. 3.4

Scolini, C., L. Rodriguez, M. Mierla, J. Pomoell, and S. Poedts, 2019. Observation-based modelling of magnetised coronal mass ejections with EUHFORIA. *Astron. Astrophys.*, **626**, A122. 10.1051/0004-6361/201935053. 1

Scolini, C., C. Verbeke, S. Poedts, E. Chané, J. Pomoell, and F. P. Zuccarello, 2018b. Effect of the Initial Shape of Coronal Mass Ejections on 3-D MHD Simulations and Geoeffectiveness Predictions. *Space Weather*, **16**(6), 754–771. 10.1029/2018SW001806. 2, 2, 3.4

Scolini, C., R. M. Winslow, N. Lugaz, and S. Poedts, 2021. Evolution of Interplanetary Coronal Mass Ejection Complexity: A Numerical Study through a Swarm of Simulated Spacecraft. *Astrophys. J. Lett.*, **916**(2), L15. 10.3847/2041-8213/ac0d58. 3

Scolini, C., R. M. Winslow, N. Lugaz, and S. Poedts, 2023. Characteristic Scales of Complexity and Coherence within Interplanetary Coronal Mass Ejections: Insights from Spacecraft Swarms in Global Heliospheric Simulations. *Astrophys. J.*, **944**(1), 46. 10.3847/1538-4357/aca893. 3

Shen, F., Y. Liu, and Y. Yang, 2021a. Numerical Research on the Effect of the Initial Parameters of a CME Flux-rope Model on Simulation Results. *Astrophys. J. Suppl.*, **253**(1), 12. 10.3847/1538-4365/abd4d2. 1

Shen, F., Y. Liu, and Y. Yang, 2021b. Numerical Research on the Effect of the Initial Parameters of a CME Flux-rope Model on Simulation Results. II. Different Locations of Observers. *Astrophys. J.*, **915**(1), 30. 10.3847/1538-4357/ac004e. 1

Shue, J. H., J. K. Chao, H. C. Fu, C. T. Russell, P. Song, K. K. Khurana, and H. J. Singer, 1997. A new functional form to study the solar wind control of the magnetopause size and shape. *J. Geophys. Res.*, **102**(A5), 9497–9512. 10.1029/97JA00196. 3.4, 7, 11

Singh, T., M. S. Yalim, N. V. Pogorelov, and N. Gopalswamy, 2020. A Modified Spheromak Model Suitable for Coronal Mass Ejection Simulations. *Astrophys. J.*, **894**(1), 49. 10.3847/1538-4357/ab845f. 1

Thernisien, A., 2011. Implementation of the Graduated Cylindrical Shell Model for the Three-dimensional Reconstruction of Coronal Mass Ejections. *Astrophys. J. Suppl.*, **194**(2), 33. 10.1088/0067-0049/194/2/33. 1

Thernisien, A., A. Vourlidas, and R. A. Howard, 2009. Forward Modeling of Coronal Mass Ejections Using STEREO/SECCHI Data. *Sol. Phys.*, **256**(1-2), 111–130. 10.1007/s11207-009-9346-5. 4

Verbeke, C., M. L. Mays, C. Kay, P. Riley, E. Palmerio, et al., 2023. Quantifying errors in 3D CME parameters derived from synthetic data using white-light reconstruction techniques. *Adv. Space Res.*, **72**(12), 5243–5262. 10.1016/j.asr.2022.08.056. 4

Vourlidas, A., B. J. Lynch, R. A. Howard, and Y. Li, 2013. How Many CMEs Have Flux Ropes? Deciphering the Signatures of Shocks, Flux Ropes, and Prominences in Coronagraph Observations of CMEs. *Sol. Phys.*, **284**(1), 179–201. 10.1007/s11207-012-0084-8. 1

Vourlidas, A., S. Patsourakos, and N. P. Savani, 2019. Predicting the geoeffective properties of coronal mass ejections: current status, open issues and path forward. *Phil. Trans. R. Soc. London Ser. A*, **377**(2148), 20180,096. 10.1098/rsta.2018.0096. 3.3, 4.3

Yurchyshyn, V., Q. Hu, R. P. Lepping, B. J. Lynch, and J. Krall, 2007. Orientations of LASCO Halo CMEs and their connection to the flux rope structure of interplanetary CMEs. *Adv. Space Res.*, **40**(12), 1821–1826. 10.1016/j.asr.2007.01.059, astro-ph/0703627. 5

677 Zhang, M., X. S. Feng, and L. P. Yang, 2019. Three-dimensional MHD simulation of the 2008 December
678 12 coronal mass ejection: from the Sun to Interplanetary space. *J. Space Weather Space Clim.*, **9**, A33.
679 10.1051/swsc/2019034. 1

680 Zhou, Y., X. Feng, and X. Zhao, 2014. Using a 3-D MHD simulation to interpret propagation and evolution
681 of a coronal mass ejection observed by multiple spacecraft: The 3 April 2010 event. *J. Geophys. Res.*
682 *Space Phys.*, **119**(12), 9321–9333. 10.1002/2014JA020347. 1